Sensing optical fibers for earthquake source characterization using raw DAS records

Claudio Strumia[1], Alister Trabattoni[2], Mariano Supino[3], Marie Baillet[4], Diane Rivet[4], and Gaetano Festa[5]

[1]University of Naples Federico II
[2]Institut De Physique Du Globe De Paris
[3]Istituto Nazionale di Geofisica e Vulcanologia
[4]Université Nice Sophia Antipolis, CNRS, IRD, Côte d'Azur Observatory
[5]Università di Napoli Federico II

September 14, 2023

SENSING OPTICAL FIBERS FOR EARTHQUAKE SOURCE CHARACTERIZATION USING RAW DAS RECORDS

Claudio Strumia[1], Alister Trabattoni[2], Mariano Supino[3], Marie Baillet[2], Diane Rivet[2], Gaetano Festa[1,3]

[1]Università di Napoli Federico II, Physics Department, Complesso University Monte S. Angelo, Napoli, Italy.

[2]Université Côte d'Azur, Observatoire de la Côte d'Azur, CNRS, IRD, Géoazur.

[3]Istituto Nazionale di Geofisica e Vulcanologia, Osservatorio Nazionale Terremoti, Roma, Italy.

Corresponding author: Claudio Strumia (claudio.strumia@unina.it)

Key Points:

- A theoretical description of strain far field radiation from a seismic rupture is introduced
- Source parameters were evaluated from strain data for earthquakes in magnitude range $0.3 - 4.3$
- DAS allows for investigation of source parameters and site effects with fine spatial resolution.

Abstract

Distributed Acoustic Sensing (DAS) is becoming a powerful tool for earthquake monitoring, providing continuous strain-rate records of seismic events along the fiber. However, the use of standard seismological techniques for earthquake source characterization requires the conversion of data in ground motion quantities. In this study we provide a new formulation for far-field strain radiation emitted by a seismic rupture, which allows to directly analyze DAS data in their

native physical quantity. This formulation naturally accounts for the complex directional sensitivity of the fiber to body waves and to the shallow layering beneath the cable. In this domain, we show that the spectral amplitude of the strain integral is related to the Fourier transform of the source time function, and its modelling allows to determine the source parameters.

We demonstrate the validity of the technique on two case-studies, where source parameters are consistent with estimates from standard seismic instruments. When analyzing events from a 1-month DAS survey in Chile, moment - corner frequency distribution clearly shows a self-similar behavior with average stress drop of $\Delta\sigma = (0.7 \pm 0.4)$MPa. The analysis of DAS data acquired in the Southern Apennines shows a dominance of the local attenuation that masks the effective corner frequency of the events. After estimating the local attenuation coefficient, we were able to retrieve the corner frequencies for the largest magnitude events in the catalog.

Overall, this approach shows the capability of DAS technology to depict the characteristic scales of seismic sources and the released moment.

Plain Language Summary

A new formulation for far-field strain radiation from seismic ruptures is derived, leading to a direct interpretation of DAS (Distributed Acoustic Sensing) data to retrieve source properties (seismic moment and source size), via a spectral modelling. This approach is validated on real data recorded in two different tectonic environments, the Chilean margin and the southern Apennines, in Italy. Despite the unique directional sensitivity and peculiar signal characteristics, we demonstrated the high potential of DAS systems in characterizing the seismic ruptures over different space scales with accuracy increased by redundancy of information from the very-high spatial resolution in the recording of seismic waves.

1 Introduction

Distributed Acoustic Sensing (DAS) is an emerging technology in seismology that allows to get continuous recordings of seismic waves along an optical fiber. DAS systems exploit phase variations in the backscattered light to record the axial strain along the fiber (Hartog, 2017). Thus, a DAS system appears as a single-component seismic array, with main advantage to have a very dense spatial coverage of sensors and a single endpoint for the collection of data, the

interrogator, which sends and receives the laser pulses to measure the strain rate. Also, the availability of existing telecom dark fibers allows to investigate environments usually difficult to monitor, such as oceanic seafloors, volcanic flanks, and geothermal areas, over distances between a few and hundreds of kilometers (e.g., Sladen et al., 2019; Currenti et al., 2021; Tsuji et al., 2021). In the recent years, DAS technology has been successfully applied to seismology for earthquake location (Nishimura et al., 2021; Piana Agostinetti et al., 2022; Sladen et al., 2019), focal mechanism determination (Li et al., 2023), seismic velocity estimation (Lellouch et al., 2019) and site effect characterization (Ajo-Franklin et al., 2019; Spica et al., 2020).

While techniques based on time picking and polarity recognition can be directly applied to strain-rate data, determination of source parameters from DAS measurements requires further development, either processing data directly in the strain-rate domain or converting them into more classical kinematic quantities.

To provide a macroscopic characterization of the source of a seismic event, one needs to determine the seismic moment, the radiated energy, the event size and the released stress drop, referred to as source parameters. Classical techniques for determination of source parameters are based on the modelling of body waves amplitude displacement spectra, that exhibit a flat level followed by a power-law fall-off (Brune, 1970; Madariaga, 1976; Kaneko & Shearer, 2014). Uncertainty in source parameters depends on the knowledge of the Green's function, with a strong correlation between the anelastic attenuation and the source spectral fall-off (Abercrombie, 1995). This correlation can be correctly handled in the computation of uncertainties, using Bayesian approaches (e.g., Supino et al., 2019) or reduced, using small earthquakes as Empirical Green's functions (EGF) (Prieto et al., 2004; Abercrombie & Rice, 2005) or data driven attenuation functions (Oth et al., 2007).

Different approaches have been proposed to apply classical strategies for source parameter estimation to DAS data, converting strain-rate data in ground motion quantities (acceleration, velocity, or displacement). When specific seismic phases dominate the DAS section, acceleration can be directly obtained from strain rate correcting for the apparent phase speed (Daley et al., 2016). The conversion to acceleration of dominant phases can be done using a slant-stack transform, that enables source parameter estimation, even in near real-time for early warning applications (Lior et al., 2021; 2023a). However, only locally dominant phases can be

correctly converted with this technique, while energy of smaller amplitude phases is smeared along the seismogram. This issue may become critical for some applications, since DAS data are more sensitive to slow, scattered waves (Trabattoni et al., 2022) and show reduced amplitude for phases travelling at high apparent speeds (Van Den Ende & Ampuero, 2021). Phase independent techniques were also developed for converting strain into ground motion quantities based on F-K rescaling (Wang et al., 2018) and space integration using deformation (Trabattoni et al., 2023). These techniques are sensitive to the rectilinearity of the cable and introduce low-frequency artifacts that must be filtered out. This may affect the low frequency content of the seismic spectra and bias the moment magnitude estimation. Nevertheless, they have been shown to provide reliable estimations of Wood-Anderson local magnitude, which requires an accurate displacement measurement above 1 Hz (Trabattoni et al., 2023).

Relative measurements of source parameters can be performed directly in the strain domain using the EGF approach, when the seismic moment of a reference event is available (Chen, 2023; Lior, 2023b). However, this technique is limited to co-located events that differ in magnitude of at least one point (Abercrombie et al., 2017). Alternative approaches exploit correlations between measurements in the strain domain and source parameters. For instance, elastodynamic energy rate from strain was shown to scale with the kinetic energy rate from seismic sensors enabling for magnitude estimation from energy (Trabattoni et al., 2022), while peak strain-rate was demonstrated to correlate with local magnitude (Yin et al., 2023).

In this study we develop a new strategy for computing source parameters in the strain-domain, deriving an analytical formulation that links the source time function with the strain. This formulation allows to evaluate the source parameters inverting strain integral amplitude spectra. The manuscript is organized as follows. In Section 2 we present the new formulation, together with the inversion strategy and the estimation of the average radiation pattern coefficients, that account for the different sensitivity of the along-fiber strain with respect to the displacement. In Section 3, the new technique is validated through an application to real data for two case studies: a 150 km-long fiber offshore Chile and a 1.1 km-long fiber buried in a dry lake inside the Irpinia Near Fault Observatory.

2 Source modelling in strain domain

2.1 Far Field source radiation

Evaluating source parameters from native DAS recordings requires a new formulation that can directly digest dynamic quantities (i.e., strain or strain rate). This formulation can be derived from the far-field radiation emitted by a seismic source and recorded at a receiver at a hypocentral distance r on the Earth's surface.

In a homogeneous medium, the far-field displacement associated with a seismic event and characterized by a source time function $I(t)$ (hereinafter referred to as STF) can be described in spherical coordinates, separating P and S contributions (Haskell, 1964):

$$\begin{aligned} u_r &= \frac{\beta^2}{4\pi\alpha^3 r} sin2\theta cos\phi \; I\left(t - \frac{r}{\alpha}\right) \\ u_\theta &= \frac{1}{4\pi\beta r} cos2\theta cos\phi \; I\left(t - \frac{r}{\beta}\right) \\ u_\phi &= \frac{1}{4\pi\beta r} cos\theta sin\phi \; I\left(t - \frac{r}{\beta}\right) \end{aligned} \tag{1}$$

Here α and β are the P- and S-wave velocities respectively, while the STF depends on the retarded time due to wave propagation from the source to the receiver. We assumed a circular crack with fixed slip direction as source model (Madariaga, 1976). The spherical coordinates (θ the colatitude; ϕ the longitude) are defined on a Cartesian reference frame W centered on the fault, where x and z are the along-slip and fault-normal directions, respectively. Here, x and z also represent the directions of the two couples of forces responsible for the earthquake rupture. The three angular functions in equation (1) are indicated respectively as $P(\theta,\phi)_P$, $P(\theta,\phi)_{SV}$, $P(\theta,\phi)_{SH}$, and correspond to the far-field components of the displacement radiation patterns.

We derived equation (1) to evaluate the strain at the receiver (see Supplementary Text S1). Ruling out the contributions that decay faster than $1/r$ (far-field approximation), we obtain:

$$\varepsilon_{rr}^{FF} = \frac{\beta^2}{4\pi\alpha^3 r} P(\theta,\phi)_P \frac{\partial I\left(t-\frac{r}{\alpha}\right)}{\partial r}$$
$$\varepsilon_{r\theta}^{FF} = \frac{1}{8\pi\beta r} P(\theta,\phi)_{SV} \frac{\partial I\left(t-\frac{r}{\beta}\right)}{\partial r} \tag{2}$$
$$\varepsilon_{r\phi}^{FF} = -\frac{1}{8\pi\beta r} P(\theta,\phi)_{SH} \frac{\partial I\left(t-\frac{r}{\beta}\right)}{\partial r}$$

where ε is the far-field strain tensor in spherical coordinates. This representation preserves the separation between P and S contributions.

Radial derivatives of the STF can be written as a function of their time derivatives:

$$\frac{\partial I\left(t-\frac{r}{c}\right)}{\partial r} = -\frac{1}{c}\frac{\partial I\left(t-\frac{r}{c}\right)}{\partial t} \tag{3}$$

where c is the wave velocity at the receiver. Replacing (3) in (2) and computing the time integral of the strain $\xi = \int \varepsilon dt$, we get

$$\xi_{rr}^{FF} = -\frac{\beta^2}{4\pi\alpha^4 r} P(\theta,\phi)_P I$$
$$\xi_{r\theta}^{FF} = -\frac{1}{8\pi\beta^2 r} P(\theta,\phi)_{SV} I \tag{4}$$
$$\xi_{r\phi}^{FF} = \frac{1}{8\pi\beta^2 r} P(\theta,\phi)_{SH} I$$

In the equation above we omitted the dependence of the STF on the retarded time. For a 1D layered model equation (4) becomes (Aki & Richards, 2002):

$$\xi_{rr}^{FF} = -\frac{\beta_S^2}{4\pi\alpha_S^3\alpha_R r} P(\theta,\phi)_P I$$
$$\xi_{r\theta}^{FF} = -\frac{1}{8\pi\beta_S\beta_R r} P(\theta,\phi)_{SV} I \tag{5}$$
$$\xi_{r\phi}^{FF} = \frac{1}{8\pi\beta_S\beta_R r} P(\theta,\phi)_{SH} I$$

with subscripts S and R indicating that the value is computed at the source and receiver locations. The strain integral is proportional to the STF as for the far-field displacement, enabling for the inversion of ξ amplitude spectra to estimate the source parameters. It is worth to note that

equation (4) shows a larger sensitivity of DAS to the shallow velocity structure beneath the cable, as compared to the displacement.

2.2 Spectral modelling

To estimate the source parameters, we transformed eq. (5) in the frequency domain, to get the spectral amplitude $\tilde{X}(\omega) = |FFT(\xi(t))|$. Separating the source term $\tilde{S}(\omega)$ from the propagation and site effect terms, respectively $\tilde{G}(\omega)$ and $\tilde{Z}(\omega)$, leads to:

$$\tilde{X}(\omega) = \tilde{G}(\omega) \cdot \tilde{S}(\omega) \cdot \tilde{Z}(\omega) \tag{6}$$

The Green's function $\tilde{G}(\omega)$ for a layered medium and a frequency independent quality factor Q^c can be written as

$$\tilde{G}(\omega) = \widetilde{K}^c A^c e^{-\left(\frac{\omega T^c(r)}{2Q^c}\right)} \tag{7}$$

$A^c(r) = 1/r$ is the geometrical spreading contribution and $T^c(r)$ is the source-receiver travel time for the selected phase c. The factor $\widetilde{K}^c$ writes:

$$\widetilde{K}^c = \frac{\bar{B}_c^{FF} F}{8\pi \rho_S^{1/2} \rho_R^{1/2} c_S^{5/2} c_R^{3/2}} \tag{8}$$

In the above formula, F is the free surface contribution, ρ the density, also evaluated at the source and receiver locations, and $\bar{B}_c^{FF}$ the mean radiation pattern that averages the directivity effects of the different cable segments along all possible fault orientations. We assume $F = 2$. The radiation pattern is discussed in detail in the next section.

For $\tilde{S}(\omega)$ we adopted a generalized Brune model:

$$\tilde{S}(\omega) = \frac{M_0}{1 + \left(\frac{\omega}{\omega_c}\right)^{\gamma}} \tag{9}$$

This function depends on the seismic moment M_0 , proportional to the plateau level of the spectrum at low frequency, the corner angular frequency ω_c that separates the long wavelengths coherently propagating away from the crack from the interfering small wavelengths, and the decay spectral fall-off γ.

Finally, the site term $\tilde{Z}(\omega)$ was assumed to follow and exponential decay (Anderson & Hough, 1984):

$$\tilde{Z}(\omega) = e^{-\frac{\omega k^c}{2}} \tag{10}$$

where k^c is local attenuation coefficient.

Following Supino et al. (2019), we inverted the amplitude spectra with a probabilistic Bayesian approach (Tarantola, 2004) where the best parameter evaluation and uncertainties come from the integration of the a-posteriori joint Probability Density Function (PDF) in the parameter space. In the general formulation of the inverse problem, we can retrieve up to 5 parameters: the source parameters M_0, $f_c = \omega_c/2\pi$ and γ (f_c is the corner frequency); the regional attenuation factor Q^c and the local attenuation coefficient k^c. The search for maximum of the PDF is performed using a basin-hopping technique on Markov chain paths (Supino et al., 2019).

2.3 Radiation pattern

The average description of the radiation pattern for the displacement (Boore & Boatwright, 1984) cannot be simply extended to fiber recorded strain, due to limited azimuthal sensitivity of the DAS. The cable allows to recover only one out of the six components of the symmetric tensor ξ, while a three-component instrument provides a complete description of the displacement. In the case of DAS, we averaged the radiation pattern over all the possible fault orientations, and also over all the possible directions of the fiber cable on Earth's surface.

A generic direction of a ray emitted from the source can be described by the take-off and azimuth angles (θ, ϕ), in the reference W centered at the hypocenter. This ray intercepts a portion of the fiber at the Earth surface, whose local orientation can be described by a different couple of angles (θ', ϕ') in the same reference frame W. To account for these new additional degrees of freedom, the average is performed over the focal sphere and all the possible directions of the fiber relatively to the source. This yields:

$$\bar{B}_c^{FF} = \frac{1}{16\pi^2} \int_0^{2\pi} \int_0^{\pi} \int_0^{2\pi} \int_0^{\pi} |A_{1i} P(\theta, \phi)_c A_{j1}^T| sin\theta sin\theta' d\theta' d\phi' d\theta d\phi \tag{11}$$

Here the matrix $\boldsymbol{A}$ accounts for the rotation of the spherical frame from (θ, ϕ) to (θ', ϕ') (see Supplementary Text S2). The terms $P_{ij,c}$ are the angular functions defined in eq. (2). The contributions associated with P and $S = (SV + SH)$ waves can be separated. The integral (11) can be evaluated numerically, leading to:

$$\begin{aligned} \bar{B}_P^{FF} &= 0.2586 \\ \bar{B}_S^{FF} &= 0.2518 \end{aligned} \tag{12}$$

As an example, we show in Figure S1 (Supplementary material) wave contributions recorded by fibers oriented along the three-coordinate axes of the reference frame W, as a function of the take-off and azimuth.

3 Data and Results

The proposed technique was applied to evaluate the source parameters on two different datasets. First, we considered DAS data recorded by a 150-km long marine telecommunication cable, located offshore the Chilean margin; then we applied the same technique to earthquakes recorded by a 1.1 km-long cable deployed in the Southern Apennines (Italy).

3.1 Submarine DAS data offshore Chile

DAS data in Chile were recorded during the month of November 2021, when an interrogator unit (OptoDAS – Alcatel Submarine Networks) was connected to a submarine fiber optic telecom cable, operated by the GTD group and linking Concón to La Serena. The DAS was able to sense 150km-long portion of the cable. A map of the cable is represented in Figure 1b. Data were processed using a gauge length of 8.16 m with a repetition rate of 625 Hz and a spatial sampling of 1.02m averaged over 4.08m. They were further decimated to a sampling rate of 125 Hz and a spatial sampling of 65.28m. In Figure 1a an example of DAS recording along the cable is shown for a $2.9M_L$ event, along with a zoom on a record from a single channel.

For the analysis, we focused on a subset of 55 events, whose local magnitude M_L ranges between 2.5 and 4.3, also recorded by the seismic network from the Centro Sismologico National (CSN). These events are representative of the magnitude and distance ranges of earthquakes occurred during the period of the experiment. Origin times from CSN catalog were used as reference times to create three-minute-long DAS records. We individuated the S-wave

arrival time on single traces using the machine learning algorithm Earthquake Transformer (EqT) (Mousavi et al., 2020).

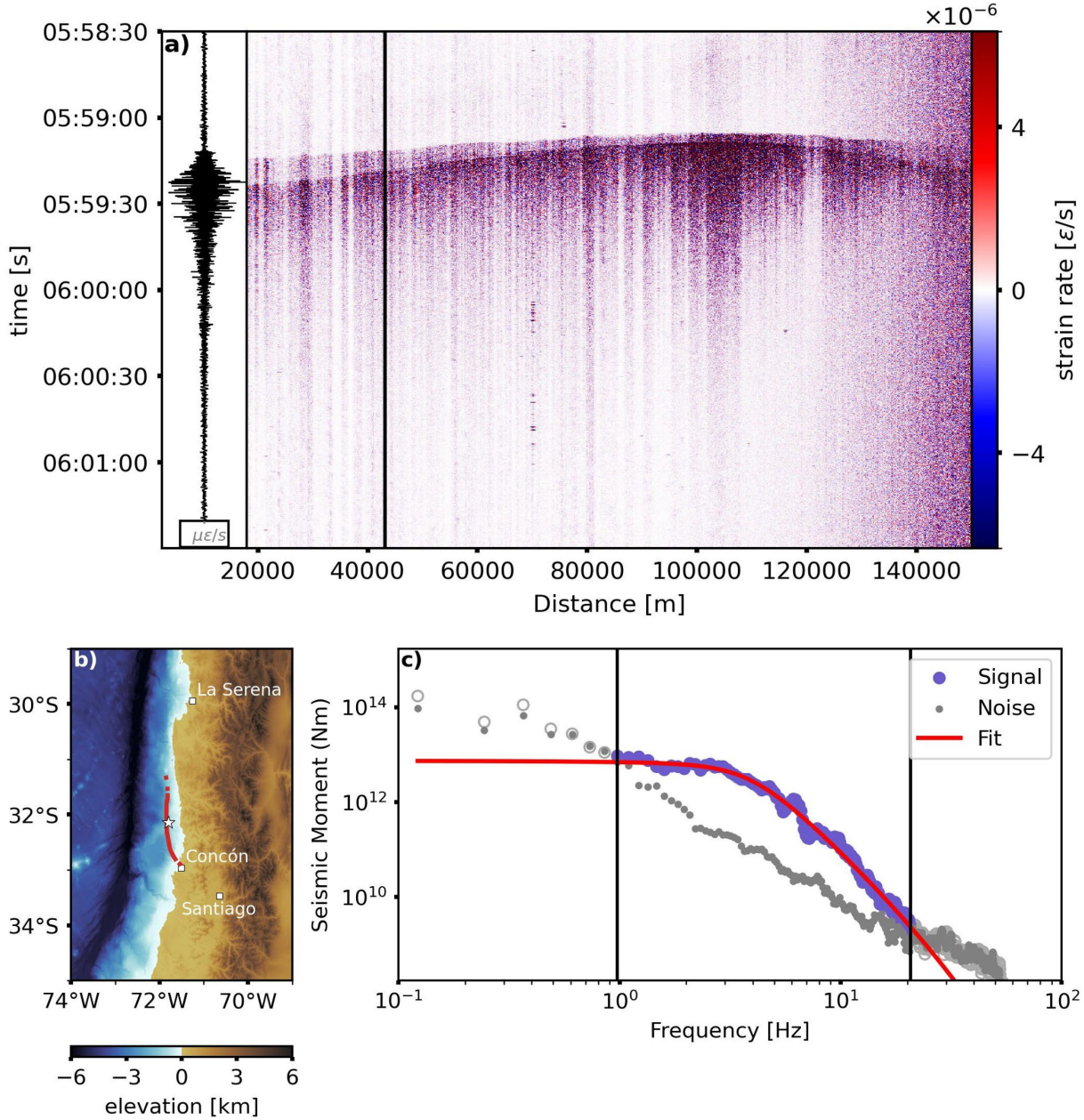

Figure 1: (a) Space-time representation of the strain rate wavefield recorded at the fiber for a $2.9M_L$ event occurred on the 2021/11/19. The black line marks the channel, whose time signal is shown on the left side. **(b)** Event location (yellow star) with respect to the fiber section used in the analysis (filled red curve). **(c)** S-wave spectrum of the selected channel (blue points, gray open circles) and of the noise (gray points) are represented. The vertical lines individuate the frequency domain where the SNR is larger than the selected threshold and the inversion was performed. The red curve is the best-fit spectrum obtained from the inversion.

The associator GaMMA (Zhu et al., 2022) was then applied to evaluate the consistency of the S-picks along the fiber, based on the apparent wave velocity. Accuracy on the picks has been shown to be sufficient for extraction of the S window for spectral analysis (Scotto di Uccio et al., 2023). The analysis focused on the inversion of S phase, which represents the dominant contribution since horizontally deployed fibers are poorly sensitive to P wave motion (Papp et al., 2017; Trabattoni et al., 2022).

Before inversion, the highest quality channels along the cable were selected based on their Signal to Noise Ratio (SNR). This latter quantity was evaluated by computing the ratio between the 90th percentile of the amplitude in a 6s window after the S arrival time, and the 90th percentile of the amplitude in a noise window of 20s before the origin time of the event. We selected channels with SNR>4, and we processed events only if the number of available channels was larger than 200, that represents almost $1/10$ of the total number of channels. Following this approach, we were able to estimate the source parameters for 37 events.

To model the spectral amplitude expressed in eq. (8) we used $c_S = 4500\ \mathrm{m/s}$ and $Q = 800$ as provided by the tomographic model of Marot et al., (2014). Also, we set $\rho_S = \rho_R = 2700\ \mathrm{kg/m^3}$ and the S-velocity at the receiver $c_R = 400\ \mathrm{m/s}$, according to the analysis of f-k diagrams. The length of the signal used to evaluate the spectra depends on the event magnitude, to account for the size dependence of the source duration (Trifunac & Brady, 1975; Supplementary TextS3). This window also contains a small portion (10%) of signal before the S-pick to account for uncertainties in the arrival times.

In Figure 1c we represent the amplitude spectrum of a channel from the DAS records. The signal exhibits a clear plateau level at low frequencies and a decay in the high frequency band. For each channel the inversion is performed in a specific frequency band (delimited in the figure by the vertical black lines), where the spectral amplitude of the signal overcomes the noise of a factor larger than 3.5. Low SNR typical of DAS recordings (Lellouch et al., 2020) results in narrower frequency band to be used for the inversion, as compared to standard seismic instruments.

Seismic moments and corner frequencies evaluated from the selected dataset exhibit self-similar behavior at almost constant stress drop (Figure 2 a). Using the relationship from Keylis-Borok, (1959):

$$\Delta\sigma = \frac{7}{16}\left(\frac{f_c}{C_k\beta}\right)^3 M_0 \tag{13}$$

and the geometrical factor of $C_k = 0.26$ from Kaneko & Shearer (2014), the averaged stress drop could be estimated to $\Delta\sigma = (0.7 \pm 0.4)$MPa. We also compared moment magnitude estimations with moment magnitude obtained from the inversion of seismic records from on land CSN stations. We found great coherency between estimates (Figure 2b). This indicates that the observed plateau level at low frequencies is representative of the event moment release and is not significantly affected by instrumental effects. Furthermore, we also compared moment magnitude obtained from DAS data with local magnitudes from CSN catalog (Supplementary TextS4) showing that our estimations are consistent with M_L and that for this range of magnitudes the low frequency plateau is coherent with the energy content of the signal.

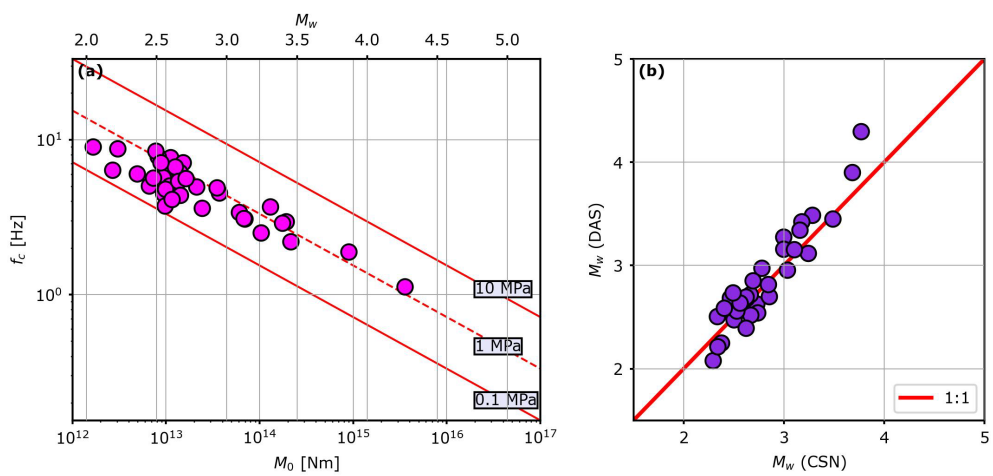

Figure 2: (a) Corner frequency as a function of the seismic moment for the Chilean dataset, exhibiting a constant stress drop scaling, with average value of (0.7 ± 0.4)MPa and values ranging between 0.1 MPa and 10 MPa. **(b)** Comparison between DAS and CSN moment magnitudes; CSN Mw are obtained from inversion of seismic from in land stations for the same dataset. Estimations exhibit a scaling consistent with a 1:1 relationship.

The consistency of the modeling of the amplitude decay with the event distance could be asserted by taking advantage of the dense spatial sampling provided by the DAS technology. For each event, we computed the residual for both M_w and f_c at each channel, by removing the average value estimated for the whole cable from the single channel estimate. We grouped residuals by hypocentral distances in bins of 1 km (from 20 to 150 km) regardless of their event or channel origin. The median and standard median absolute deviations for residuals were computed for each bin as a function of the hypocentral distance (Fig. 3). The estimations are

unbiased in the whole distance range. Only for distances below $40km$ the moment magnitude exhibits residuals slightly larger than zero; this overestimation of the geometrical spreading correction could be ascribed to possible uncertainty in event location.

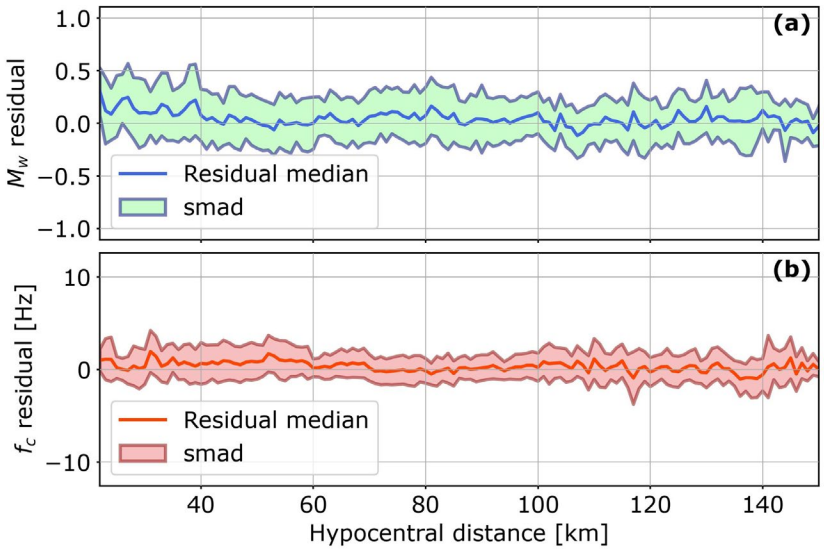

Figure 3: Analysis of the source parameters residuals as a function of the hypocentral distance. Bold lines represent the median of the residuals for each distance bin, while the error is represented as the Standard Median Absolute Deviation (SMAD). **(a)** M_w residuals exhibit a slight bias at short distances (<40 km), while no other trend is evident at other distances. **(b)** f_c residuals are unbiased, showing that the exponential decay as a model for regional attenuation well describes the spectral decay for a wide range of hypocentral distances.

3.2 Southern Apennines DAS measurements

In contrast to Chilean events, the Southern Italy DAS survey focused on smaller microseismic events ($M_L \leq 2.5$), that represent a challenging test for the resolution of source parameters. The data were acquired during a 5-month experiment, involving a DAS interrogator (Febus A1-r) connected to a 1.1km-long L-shaped fiber optic cable, buried into a shallow trench ($0.3\text{m} - 1.0\text{m}$) in a dry lake near the town of Colliano (Fig. 4b). The instrument was set to work with a sampling rate of 200Hz, further downsampled to 100Hz, and a spatial sampling of 2.4m, with a gauge length of 4.8m (see more details in Trabattoni et al. (2022)).

The site of the installation was near the emergence of the main segment of the normal fault system that generated the devastating 1980 M 6.9 Irpinia earthquake in the Southern Apennines. The area is nowadays monitored by the Irpinia Near Fault Observatory (INFO), (Chiaraluce et al., 2022) that detected several dozens of events during the deployment period

(Fig. 4a). Figure 5 shows the recordings of a $M_L 2.3$ event occurred on 2021/09/20 at 13:07:55 and reveals the specific propagation pattern due to the shallow sedimentary layering, as described in Trabattoni et al. (2022).

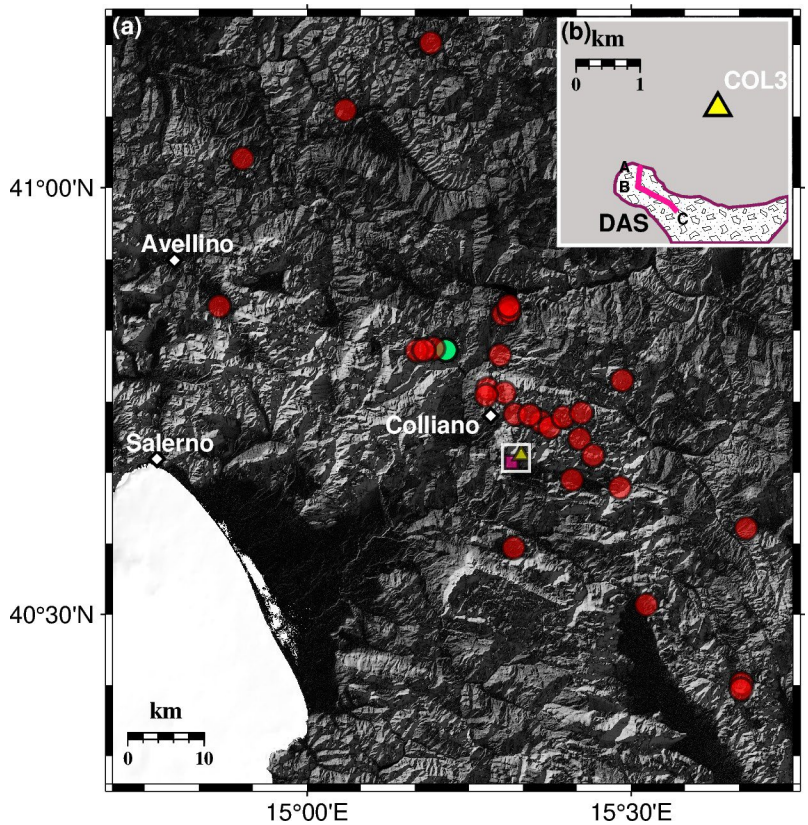

Figure 4*:* (a) Map showing the location of the fiber (white square) and the events recorded during the survey (red circles). The green point marks the event represented in Figure 5 (almost $20km$ away from the installation site). Panel **(b)** depicts the area contained in the white square, showing the L-shaped fiber (magenta line), with a kink in B, and the nearest INFO station COL3 (yellow triangle), located at less than $2km$ from the interrogator. The white-pattern area represents the dry lake where the cable was buried for the experiment.

As for the Chilean dataset, we considered events in the local bulletin (M_L from 0.3 to 2.3 and epicentral distances up to $\sim 60km$ from the interrogator unit) and extracted related DAS waveforms from the continuous data-stream. We selected the highest quality channels in the AC section of the cable following a procedure similar to what was described for the previous dataset.

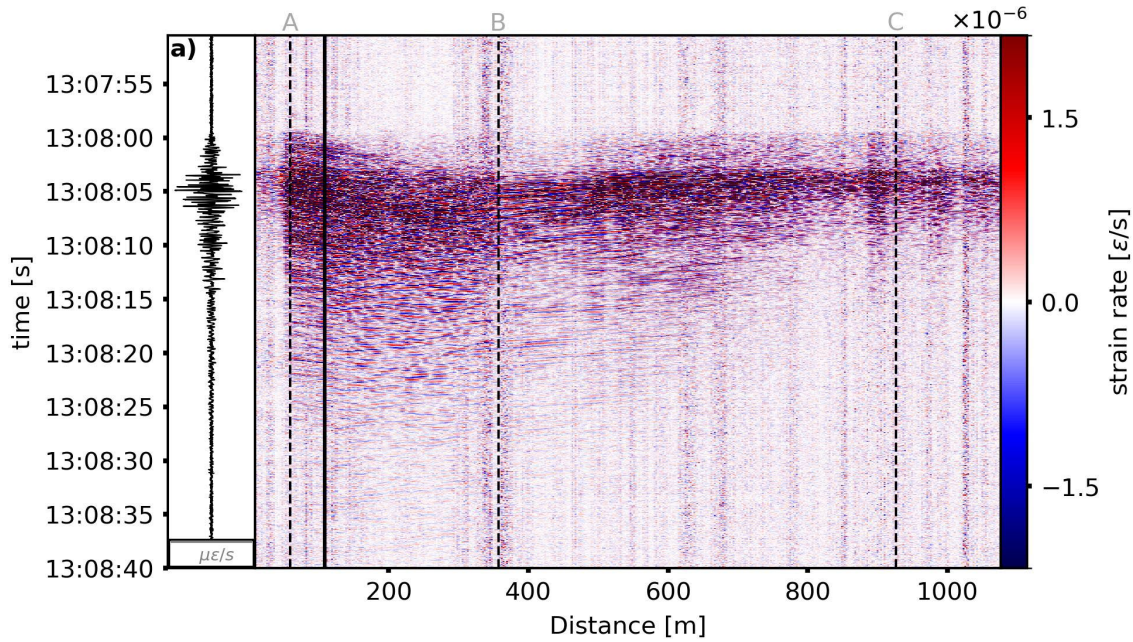

Figure 5*:* The space-time representation of the strain rate wavefield recorded by the DAS system for a M_L2.3 event occurred on 2021/09/20. The black filled line marks the channel, whose time signal is shown on the left side, while the dashed black lines individuate specific points along the cable, shown in Figure 4b.

For this dataset, we evaluated the source parameters for channels satisfying SNR>8 for 26 events that meet that criterion for at least at 40 channels. We selected 5s time windows around the S-pick (from 0.5s before to 4.5s after the S-pick) of a nearby station (COL3, distance from the fiber < $2km$, see Figure 4b) to compute the amplitude spectra.

By analyzing the spectra of the events along the fiber, we observed that the spectral decay following the plateau level starts around an apparent corner frequency of $5.5Hz$ (Figure 7b), irrespective of the event magnitude and location and of the channel along the fiber (Fig. 6a and 7a). This decay can be ascribed to local site effects that are dominant in the spectral behavior because spectral decays due to the source and to the anelastic attenuation are both expected to show a cut-off frequency dependent on magnitude (source contribution) and distance (regional anelastic attenuation). Moreover, assuming an average values of the quality factor Q for the area ($Q = 230$; Zollo et al., 2014;Amoroso et al., 2017) the spectral decay due to the anelastic attenuation is generally expected to start at frequencies higher than $5.5Hz$ for the range of hypocentral distances associated with events recorded at the fiber.

We modelled the local site effects using the local attenuation coefficient k^c, as described in eq. (10) (Anderson & Hough, 1984; Butcher et al., 2020; Ktenidou et al., 2014, 2015). To infer an average value for k^c, we selected small magnitude events in the dataset ($M_w < 1.8$) for which the source corner frequency is expected to be much larger than the observed cut-off frequency (Zollo et al., 2014). For these events, after removal of regional anelastic attenuation assuming $Q = 230$, we fit the logarithm of the amplitude spectra as a function of the frequency to evaluate k^c for each channel and each event (Figure 6a). In Figure 6b, we represent the spatial variability of k^c along the fiber. The local attenuation coefficient has its maximum in the central section of the cable, decreasing almost linearly toward the ends of the cable, and possibly mimicking the shape of the lake basement. We computed the median and the SMAD values from k^c single-channel averages, leading to $\bar{k}^c = (0.08 \pm 0.02)$s.

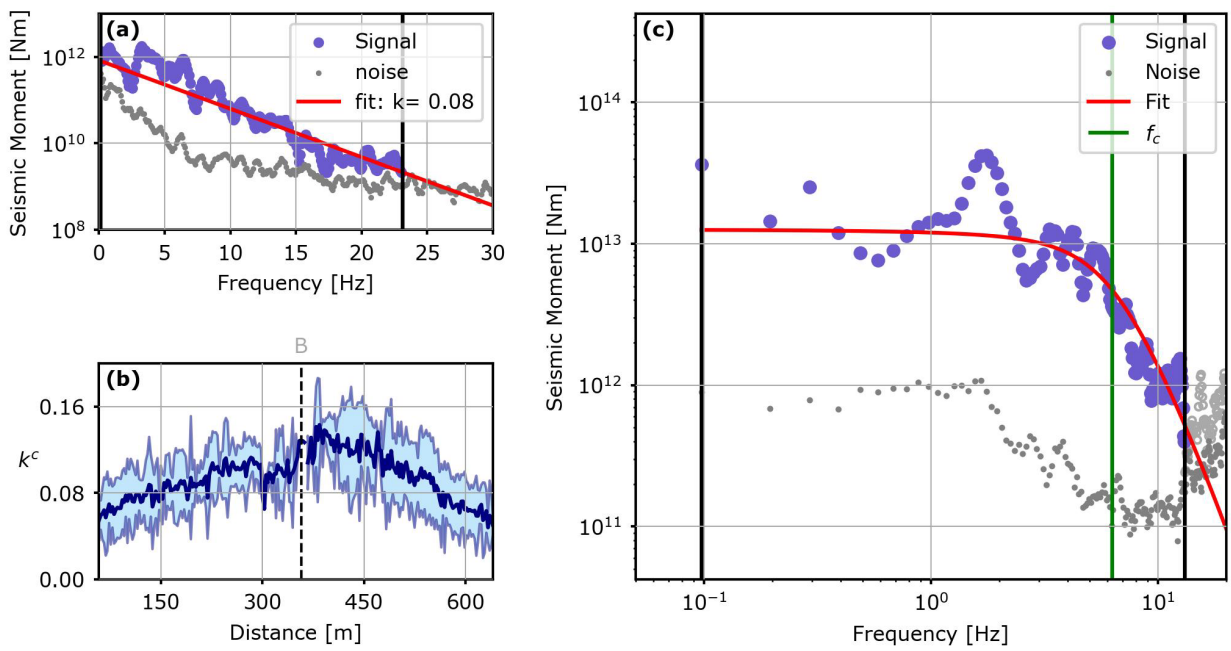

Figure 6*:* **(a)** Example of the linear fit (red curve) estimated on the log-linear spectrum (blue circles) at a specific channel of the fiber to obtain a single-channel estimate of k^c. The spectrum is fitted in the frequency band where the SNR exceeds the imposed threshold of 3.5 (black vertical bars). **(b)** k^c variability along the cable by the mean of average (blue bold curve) and standard deviation (shaded area). The dashed black line individuates the position where the cable kinks (Figure 4b). **(c)** Log-log spectrum at a fixed channel for a M_L2.2 event recorded on the fiber on the 2023/11/04 with the same color code described in Figure 1. The f_c estimation is marked by a vertical green line.

The latter value was used in the source inversion of the largest magnitude events ($M_w > 1.8$) to remove local site effects from their observed spectra, thereby evaluating their seismic moment and source corner frequency.

We compared source parameters estimation from DAS and INFO network seismic records (Figure 7). M_w estimations from DAS are found to be consistent with the ones retrieved from the INFO network, obtained inverting local seismic records (Fig. 7a). The correlation between both estimates is lower than in the Chilean case. For Southern Apennines, this can be attributed to the short length of the cable that does not capture the variability of the M_w estimates due the distance and azimuth. Corner frequencies recovered from DAS saturate at 5.5 Hz without the site correction (gray dots) but are compatible with the ones obtained from INFO seismic stations when modelling the site attenuation (green dots, Fig. 7b).

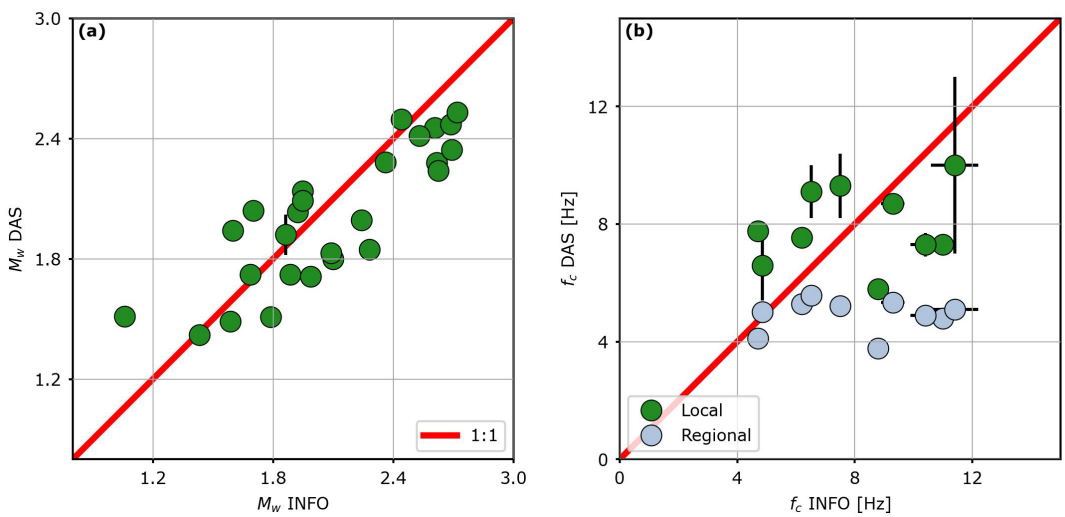

Figure7: (a) Moment magnitude comparison between estimates from DAS and from INFO network. Moment magnitude estimated from DAS data follows a 1:1 scaling (red line) with standard seismic station results. **(b)** Corner frequency comparison between DAS and local network. Without correction for local site effects (gray dots) DAS estimates saturate resulting in an apparent f_c around $5.5Hz$. After the correction for local site effects (green dots), the two estimates become comparable.

4 Discussions

The new formulation of the far field strain spectra developed in this work does not require to convert waveforms from strain to velocity (e.g., Wang et al., 2018; Lior et al., 2021;

Trabattoni et al., 2023) and can be directly applied to raw DAS data. Signal manipulation during the conversion to kinematic quantities could modify the seismic spectra. For example, the low-wavenumber accuracy of the conversion of the strain rate to displacement by direct integration is limited by the rectilinearity of the fiber (Trabattoni et al., 2023). Also, the use of the slant-stack transform for the evaluation of the dominant apparent velocity (Lior et al., 2021, 2023a), only allows to correctly convert the most energetic phase, and the spurious contribution of other not well-integrated, superimposing phases cannot be easily evaluated. The proposed strategy also disengages from the colocation hypothesis and the knowledge of parameters for a reference event, as required for EGF based approaches (Chen, 2023; Lior, 2023b) that also rely on raw DAS data.

From the theoretical formulation, we retrieve an enhanced sensitivity of strain measurements to the shallow structure beneath the cable, with a dependence on the wave velocity at three-halves power instead of one-half, as compared to the displacement formulation. Knowledge of a-priori shallow S (and P) wave velocities is thus relevant to avoid biases in the estimation of the seismic moment. It is worth to note that this velocity also enters (as apparent velocity) in the conversion from strain-rate to acceleration (Daley et al., 2016).

We also report average radiation pattern contributions which are more than twice smaller than the ones retrieved for seismometer records, in agreement to the lower and complex directional sensitivity of DAS to body waves (Martin et al., 2021). Moreover, the presence of additional nodes in the radiation pattern diagrams suggests cable deployments with changes in the fiber orientation, to improve the resolution in the source parameters.

Finally, the proposed approach, when integrated in a probabilistic formulation, can be fully automated, with the quality of the solutions based on the shape of the a-posteriori probability density functions (Supino et al., 2019). Also, when extending this approach to the P-waves, this strategy could be applied in real-time, when few seconds of early P wave signal are available (e.g., Caprio et al., 2011).

Validation of this approach on Chilean dataset ($M_L = 2.6 - 4.3$) shows a reliable estimation of source parameters, comparable with results from standard seismometers. We do not observe any dependence of parameters on the hypocentral distance, showing that attenuation correction is consistent throughout the whole cable, enabling DAS to characterize the source of

events in wide range of hypocentral distances. Moreover, source parameters exhibit self-similar behavior with a mean stress drop of $0.7 \pm 0.4MPa$, consistent with the values retrieved for events in Central Chile (Şen et al., 2015).

In the second application we estimated source parameters for smaller size events ($M_L = 0.3 - 2.3$), using DAS data recorded on a much shorter ($1.1km$) cable installed in the active tectonic environment of Southern Apennines (Italy). We found good agreement for moment magnitude estimates from DAS as compared to the ones from standard seismic stations. Because of the specific installation site (a dry lake), local attenuation plays a crucial role, masking the effect of the source size in the spectrum. Using a parametric EGF-based approach, we estimated an average local attenuation coefficient $\bar{k}^c = (0.08 \pm 0.02)$ s that is comparable with the values estimated in very soft soils (Ktenidou et al., 2015). Also, the analysis of the variability of k^c shows linear trends with distance along the cable, coherent with the increase in attenuation with the distances from the tips of the basin (Trabattoni et al., 2022), and that can be correlated with the depth of the basin (Campbell, 2009). This indicates the possibility to use DAS to infer mechanical properties of the shallow layering, beyond the source parameters. When removing this attenuation from the spectra of the largest magnitude events in the catalog, we were able to resolve the corner frequencies, that now result to be coherent with the estimates from velocity seismograms.

Working with DAS spectral amplitudes, especially for time integrated strain data, displays unique instrumental noise, with coherent low frequency contribution that tightens the bandwidth where the signal can be inverted (Lior et al., 2023a). This issue is related to instrumental properties rather than seismic information in the signal, and could be mitigated with the evolution and increasing demand of distributed sensing sensors. However, for events for which we estimated both seismic moment and event size (M_w between 2.0 and 4.3) we report that the corner frequency lies in the middle of the frequency band available for the inversion, allowing for an accurate estimation of source parameters. This is demonstrated by the comparison with results from standard seismic instruments. For smaller magnitude events, we were able to capture only the flat level of the spectrum, preventing from the estimate of earthquake size. We might also expect a limitation in the use of DAS data for source parameter estimation for events with magnitude larger than $4.5 - 5.0$ (not included in the analyzed

catalogs), where the expected corner frequency approaches the lower limit of the informative frequency bandwidth. In this case, the inversion could provide biased estimates for the moment magnitude, as compared to standard instruments.

Consistency of estimates between DAS and seismic data guarantees that the contribution of secondary phases in the selected S-wave window, to which the DAS could be more sensitive, does not introduce significant biases in the retrieved source parameters.

5 Conclusions

In this work we estimated source parameters from a spectral inversion of DAS data in their native representation, based on a novel formulation describing the far-field radiation in the strain domain. The theoretical modeling displays an enhanced sensitivity to the velocity structure beneath the cable and the radiation pattern.

Including this model in a probabilistic framework for the inversion (Supino et al., 2019) allowed us to estimate the moment magnitude and the corner frequency from two different datasets, showing consistent values when compared to authoritative catalogs.

When analyzing data acquired from a $150km$ ocean-bottom dark fiber cable near the Chilean trench ($M_L = 2.6 - 4.3$), we found a self-similar behavior of the seismicity with an mean stress drop of $0.7 \pm 0.4MPa$. Despite their natural variability, we report no biases of average estimations of source parameters with hypocentral distance along the cable.

Application of the technique to microseismic data ($M_L = 0.3 - 2.3$) acquired in the Southern Apennines (Italy) represent a challenging test for the achievable resolution in the characterization of small earthquakes using DAS. We coherently estimated the seismic moment in the whole magnitude interval. Site effects were shown to dominate the high frequency part of the spectrum and need to be modelled and corrected for to retrieve the source extension.

The two case studies presented in this work reveal the high potential of DAS for source characterization, while the dense spatial sampling could be a key ingredient for understanding source parameters variability and their relationship with the rupture behavior and the local structure. Nonetheless, fiber optic data require careful processing both for the peculiar signal properties, and for the large amount of data that requires efficient storage and processing.

Acknowledgments

Chilean data have been retrieved in the framework of the project funded by the European Research Council (ERC) under the European Union's Horizon 2020 research and innovation programme (grant agreement No. 101041092).

Data Availability Statement

The strain rates of the Chilean earthquakes and seismic traces from CSN used in this article are available at the link: https://doi.org/10.5281/zenodo.8340063 (Rivet et al., 2023). DAS waveforms from the Southern Apennines dataset are available at: https://doi.org/10.5281/zenodo.8337580 (Strumia et al., 2023). Seismic data from Chilean seismic station can be accessed through the from IRISDMC (http://ds.iris.edu/mda/), network code C1. Products from INFO network can be accessed through the Irpinia Seismic Network infrastructure (ISNet: https://isnet.unina.it). Seismic data can be accessed through EIDA portal (https://eida.ingv.it/it/, network code IX).

Catalog of the analyzed events and codes used to produce the Figures in the paper are available on GitHub (https://github.com/ClaudioStrumia). Figures were made using matplotlib version 3.6.3. Map in Figure 4 was made using PyGMT (Uieda et al., 2021) using Generic Mapping Tools (GMT) version 6 (Wessel et al., 2019).

Supporting Information summary

Text S1 to S4

Figures S1 to S2

References

Abercrombie, R. E. (1995). Earthquake source scaling relationships from −1 to 5 ML using seismograms recorded at 2.5-km depth. *Journal of Geophysical Research: Solid Earth*, *100*(B12), 24015–24036. https://doi.org/10.1029/95JB02397

Abercrombie, R. E., Bannister, S., Ristau, J., & Doser, D. (2017). Variability of earthquake stress drop in a subduction setting, the Hikurangi Margin, New Zealand. *Geophysical Journal International*, *208*(1), 306–320. https://doi.org/10.1093/gji/ggw393

Abercrombie, R. E., & Rice, J. R. (2005). Can observations of earthquake scaling constrain slip weakening? In *Geophysical Journal International* (Vol. 162, Issue 2, pp. 406–424). https://doi.org/10.1111/j.1365-246X.2005.02579.x

Ajo-Franklin, J. B., Dou, S., Lindsey, N. J., Monga, I., Tracy, C., Robertson, M., Rodriguez Tribaldos, V., Ulrich, C., Freifeld, B., Daley, T., & Li, X. (2019). Distributed Acoustic Sensing Using Dark Fiber for Near-Surface Characterization and Broadband Seismic Event Detection. *Scientific Reports*, *9*(1). https://doi.org/10.1038/s41598-018-36675-8

Aki, K., & Richards, P. G. (2002). *Quantitative seismology*.

Amoroso, O., Russo, G., De Landro, G., Zollo, A., Garambois, S., Mazzoli, S., Parente, M., & Virieux, J. (2017). From velocity and attenuation tomography to rock physical modeling: Inferences on fluid-driven earthquake processes at the Irpinia fault system in southern Italy. *Geophysical Research Letters*, *44*(13), 6752–6760. https://doi.org/10.1002/2016GL072346

Anderson, J. G., & Hough, S. E. (1984). A model for the shape of the Fourier amplitude spectrum of acceleration at high frequencies. In *Bulletin of the Seismological Society of America* (Vol. 74, Issue 5).

Arthur H. Hartog. (2017). *An introduction to distributed optical fibre sensors* (A. H. Hartog, Ed.). CRC Press.

Boore, D. M., & Boatwright, J. (1984). Average body-wave radiation coeffiecients. In *Bulletin of the Seismological Society of America* (Vol. 74, Issue 5).

Brune, J. N. (1970). Tectonic stress and the spectra of seismic shear waves from earthquakes. *Journal of Geophysical Research*, *75*(26), 4997–5009. https://doi.org/10.1029/JB075i026p04997

Butcher, A., Luckett, R., Kendall, J. M., & Baptie, B. (2020). Seismic magnitudes, corner frequencies, and microseismicity: Using ambient noise to correct for high-frequency attenuation. *Bulletin of the Seismological Society of America*, *110*(3), 1260–1275. https://doi.org/10.1785/0120190032

Campbell, K. W. (2009). Estimates of Shear-Wave Q and κ0 for unconsolidated and semiconsolidated sediments in Eastern North America. *Bulletin of the Seismological Society of America*, *99*(4), 2365–2392. https://doi.org/10.1785/0120080116

Caprio, M., Lancieri, M., Cua, G. B., Zollo, A., & Wiemer, S. (2011). An evolutionary approach to real-time moment magnitude estimation via inversion of displacement spectra. *Geophysical Research Letters*, *38*(2). https://doi.org/10.1029/2010GL045403

Chen, X. (2023). Source parameter analysis using distributed acoustic sensing - an example with the PoroTomo array. *Geophysical Journal International*, *233*(3), 2207–2213. https://doi.org/10.1093/gji/ggad061

Chiaraluce, L., Festa, G., Bernard, P., Caracausi, A., Carluccio, I., Clinton, J. F., Di Stefano, R., Elia, L., Evangelidis, C. P., Ergintav, S., Jianu, O., Kaviris, G., Marmureanu, A., Šebela, S., & Sokos, E. (2022). The Near Fault Observatory community in Europe: a new resource for faulting and hazard studies. *Annals of Geophysics*, *65*(3), 1–17. https://doi.org/10.4401/ag-8778

Currenti, G., Jousset, P., Napoli, R., Krawczyk, C., & Weber, M. (2021). On the comparison of strain measurements from fibre optics with a dense seismometer array at Etna volcano (Italy). *Solid Earth*, *12*(4), 993–1003. https://doi.org/10.5194/se-12-993-2021

Daley, T. M., Miller, D. E., Dodds, K., Cook, P., & Freifeld, B. M. (2016). Field testing of modular borehole monitoring with simultaneous distributed acoustic sensing and geophone vertical seismic profiles at Citronelle, Alabama. *Geophysical Prospecting*, *64*(5), 1318–1334. https://doi.org/10.1111/1365-2478.12324

Haskell, N. A. (1964). Total energy and energy spectral density of elastic wave radiation from propagating faults. *Bulletin of the Seismological Society of America*, *54*(6A), 1811–1841. https://doi.org/10.1785/BSSA05406A1811

Kaneko, Y., & Shearer, P. M. (2014). Seismic source spectra and estimated stress drop derived from cohesive-zone models of circular subshear rupture. *Geophysical Journal International*, *197*(2), 1002–1015. https://doi.org/10.1093/gji/ggu030

Keylis-Borok, V. (1959). On estimation of the displacement in an earthquake source and of source dimensions. *Annals of Geophysics*, *12*(2).

Ktenidou, O. J., Abrahamson, N. A., Drouet, S., & Cotton, F. (2015). Understanding the physics of kappa (κ): Insights from a downhole array. *Geophysical Journal International*, *203*(1), 678–691. https://doi.org/10.1093/gji/ggv315

Ktenidou, O. J., Cotton, F., Abrahamson, N. A., & Anderson, J. G. (2014). Taxonomy of κ: A review of definitions and estimation approaches targeted to applications. *Seismological Research Letters*, *85*(1), 135–146. https://doi.org/10.1785/0220130027

Lellouch, A., Lindsey, N. J., Ellsworth, W. L., & Biondi, B. L. (2020). Comparison between distributed acoustic sensing and geophones: Downhole microseismic monitoring of the FORGE geothermal experiment. *Seismological Research Letters*, *91*(6), 3256–3268. https://doi.org/10.1785/0220200149

Lellouch, A., Yuan, S., Spica, Z., Biondi, B., & Ellsworth, W. L. (2019). Seismic Velocity Estimation Using Passive Downhole Distributed Acoustic Sensing Records: Examples From the San Andreas Fault Observatory at Depth. *Journal of Geophysical Research: Solid Earth*, *124*(7), 6931–6948. https://doi.org/10.1029/2019JB017533

Li, J., Zhu, W., Biondi, E., & Zhan, Z. (2023). Earthquake focal mechanisms with distributed acoustic sensing. *Nature Communications*, *14*(1), 4181. https://doi.org/10.1038/s41467-023-39639-3

Lior, I. (2023). *Accurate Magnitude and Stress Drop using the Empirical Green's Function Method Applied to Distributed Acoustic Sensing*. https://doi.org/https://doi.org/10.22541/essoar.169008302.27323942/v1

Lior, I., Rivet, D., Ampuero, J. P., Sladen, A., Barrientos, S., Sánchez-Olavarría, R., Villarroel Opazo, G. A., & Bustamante Prado, J. A. (2023). Magnitude estimation and ground motion prediction to harness fiber optic distributed acoustic sensing for earthquake early warning. *Scientific Reports*, *13*(1). https://doi.org/10.1038/s41598-023-27444-3

Lior, I., Sladen, A., Mercerat, D., Ampuero, J. P., Rivet, D., & Sambolian, S. (2021). Strain to ground motion conversion of distributed acoustic sensing data for earthquake magnitude and stress drop determination. *Solid Earth*, *12*(6), 1421–1442. https://doi.org/10.5194/se-12-1421-2021

Madariaga, R. (1976). Dynamics of an expanding circular fault. *Bulletin of the Seismological Society of America*, *66*(3), 639–666. https://doi.org/10.1785/bssa0660030639

Marot, M., Monfret, T., Gerbault, M., Nolet, G., Ranalli, G., & Pardo, M. (2014). Flat versus normal subduction zones: A comparison based on 3-D regional traveltime tomography and petrological modelling of central Chile and western Argentina (29°-35°S). *Geophysical Journal International*, *199*(3), 1633–1654. https://doi.org/10.1093/gji/ggu355

Martin, E. R., Lindsey, N. J., Ajo-Franklin, J. B., & Biondi, B. L. (2021). Introduction to Interferometry of Fiber-Optic Strain Measurements. In *Distributed Acoustic Sensing in Geophysics: Methods and Applications* (pp. 113–129). wiley. https://doi.org/10.1002/9781119521808.ch09

Mousavi, S. M., Ellsworth, W. L., Zhu, W., Chuang, L. Y., & Beroza, G. C. (2020). Earthquake transformer—an attentive deep-learning model for simultaneous earthquake detection and phase picking. *Nature Communications*, *11*(1). https://doi.org/10.1038/s41467-020-17591-w

Nishimura, T., Emoto, K., Nakahara, H., Miura, S., Yamamoto, M., Sugimura, S., Ishikawa, A., & Kimura, T. (2021). Source location of volcanic earthquakes and subsurface characterization using fiber-optic cable and distributed acoustic sensing system. *Scientific Reports*, *11*(1). https://doi.org/10.1038/s41598-021-85621-8

Oth, A., Bindi, D., Parolai, S., & Wenzel, F. (2007). *S-Wave Attenuation Characteristics Beneath the Vrancea Region (Romania)-New Insights from the Inversion of Ground Motion Spectra*.

Papp, B., Donno, D., Martin, J. E., & Hartog, A. H. (2017). A study of the geophysical response of distributed fibre optic acoustic sensors through laboratory-scale experiments. *Geophysical Prospecting*, *65*(5), 1186–1204. https://doi.org/10.1111/1365-2478.12471

Piana Agostinetti, N., Villa, A., & Saccorotti, G. (2022). Distributed acoustic sensing as a tool for subsurface mapping and seismic event monitoring: A proof of concept. *Solid Earth*, *13*(2), 449–468. https://doi.org/10.5194/se-13-449-2022

Prieto, G. A., Shearer, P. M., Vernon, F. L., & Kilb, D. (2004). Earthquake source scaling and self-similarity estimation from stacking P and S spectra. *Journal of Geophysical Research: Solid Earth*, *109*(8). https://doi.org/10.1029/2004JB003084

Rivet, D., Trabattoni, A., & Baillet, M. (2023). DAS Chile waveforms [Data set]. Zenodo. https://doi.org/10.5281/zenodo.8340063

Scotto di Uccio, F., Scala, A., Festa, G., Picozzi, M., & Beroza, G. C. (2023). Comparing and integrating artificial intelligence and similarity search detection techniques: application to seismic sequences in Southern Italy. *Geophysical Journal International*, *233*(2), 861–874. https://doi.org/10.1093/gji/ggac487

Şen, A. T., Cesca, S., Lange, D., Dahm, T., Tilmann, F., & Heimann, S. (2015). Systematic Changes of Earthquake Rupture with Depth: A Case Study from the 2010 Mw8.8 Maule, Chile, Earthquake Aftershock Sequence. *Bulletin of the Seismological Society of America*, *105*(5), 2468–2479. https://doi.org/10.1785/0120140123

Sladen, A., Rivet, D., Ampuero, J. P., De Barros, L., Hello, Y., Calbris, G., & Lamare, P. (2019). Distributed sensing of earthquakes and ocean-solid Earth interactions on seafloor telecom cables. *Nature Communications*, *10*(1). https://doi.org/10.1038/s41467-019-13793-z

Spica, Z. J., Perton, M., Martin, E. R., Beroza, G. C., & Biondi, B. (2020). Urban Seismic Site Characterization by Fiber-Optic Seismology. *Journal of Geophysical Research: Solid Earth*, *125*(3). https://doi.org/10.1029/2019JB018656

Strumia, C., Festa, G., & Trabattoni, A. (2023). DAS Irpinia waveforms [Data set]. Zenodo. https://doi.org/10.5281/zenodo.8337580

Supino, M., Festa, G., & Zollo, A. (2019). A probabilistic method for the estimation of earthquake source parameters from spectral inversion: Application to the 2016-2017 Central Italy seismic sequence. *Geophysical Journal International*, *218*(2), 988–1007. https://doi.org/10.1093/gji/ggz206

Tarantola, A. (2004). *Inverse Problem Theory and Methods for Model Parameter Estimation*.

Trabattoni, A., Biagioli, F., Strumia, C., Van Den Ende, M., Scotto Di Uccio, F., Festa, G., Rivet, D., Sladen, A., Ampuero, J. P., Métaxian, J.-P., & Stutzmann, É. (2023). *From*

strain to displacement: using deformation to enhance distributed acoustic sensing applications. https://doi.org/http://dx.doi.org/10.31223/X5ZD3C

Trabattoni, A., Festa, G., Longo, R., Bernard, P., Plantier, G., Zollo, A., & Strollo, A. (2022). Microseismicity Monitoring and Site Characterization With Distributed Acoustic Sensing (DAS): The Case of the Irpinia Fault System (Southern Italy). *Journal of Geophysical Research: Solid Earth*, *127*(9). https://doi.org/10.1029/2022JB024529

Trifunac, M. D., & Brady, A. G. (1975). A study on the duration of strong earthquake ground motion. In *Bulletin of the Seismological Society of America* (Vol. 65, Issue 3).

Tsuji, T., Ikeda, T., Matsuura, R., Mukumoto, K., Hutapea, F. L., Kimura, T., Yamaoka, K., & Shinohara, M. (2021). Continuous monitoring system for safe managements of CO2 storage and geothermal reservoirs. *Scientific Reports*, *11*(1). https://doi.org/10.1038/s41598-021-97881-5

Uieda, L., Tian, D., Leong, W. J., Toney, L., Schlitzer, W., Yao, J., Grund, M., Jones, M., Materna, K., Newton, T., Ziebarth, M., & Wessel, P. (2021). PyGMT: A Python interface for the Generic Mapping Tools (v0.3.1) [Software]. Zenodo. https://doi.org/10.5281/zenodo.4592991

Van Den Ende, M. P. A., & Ampuero, J. P. (2021). Evaluating seismic beamforming capabilities of distributed acoustic sensing arrays. *Solid Earth*, *12*(4), 915–934. https://doi.org/10.5194/se-12-915-2021

Wang, H. F., Zeng, X., Miller, D. E., Fratta, D., Feigl, K. L., Thurber, C. H., & Mellors, R. J. (2018). Ground motion response to an ML 4.3 earthquake using co-located distributed acoustic sensing and seismometer arrays. *Geophysical Journal International*, *213*(3), 2020–2036. https://doi.org/10.1093/GJI/GGY102

Wessel, P., Luis, J. F., Uieda, L., Scharroo, R., Wobbe, F., Smith, W. H. F., & Tian, D. (2019). The Generic Mapping Tools Version 6. *Geochemistry, Geophysics, Geosystems*, *20*(11), 5556–5564. https://doi.org/10.1029/2019GC008515

Yin, J., Zhu, W., Li, J., Biondi, E., Miao, Y., Spica, Z. J., Viens, L., Shinohara, M., Ide, S., Mochizuki, K., Husker, A. L., & Zhan, Z. (2023). Earthquake Magnitude With DAS: A Transferable Data-Based Scaling Relation. *Geophysical Research Letters*, *50*(10). https://doi.org/10.1029/2023GL103045

Zhu, W., McBrearty, I. W., Mousavi, S. M., Ellsworth, W. L., & Beroza, G. C. (2022). Earthquake Phase Association Using a Bayesian Gaussian Mixture Model. *Journal of Geophysical Research: Solid Earth*, *127*(5). https://doi.org/10.1029/2021JB023249

Zollo, A., Orefice, A., & Convertito, V. (2014). Source parameter scaling and radiation efficiency of microearthquakes along the Irpinia fault zone in southern Apennines, Italy. *Journal of Geophysical Research: Solid Earth*, *119*(4), 3256–3275. https://doi.org/10.1002/2013JB010116